




Oxygen vacancy-driven orbital multichannel Kondo effect in Dirac nodal line metals IrO_2 and RuO_2

Sheng-Shiuan Yeh^{1,2,3}, Ta-Kang Su¹, An-Shao Lien¹, Farzaneh Zamani⁴, Johann Kroha ⁴, Chao-Ching Liao¹, Stefan Kirchner ^{5,6}✉ & Juhn-Jong Lin ^{1,2,7}✉

Strong electron correlations have long been recognized as driving the emergence of novel phases of matter. A well recognized example is high-temperature superconductivity which cannot be understood in terms of the standard weak-coupling theory. The exotic properties that accompany the formation of the two-channel Kondo (2CK) effect, including the emergence of an unconventional metallic state in the low-energy limit, also originate from strong electron interactions. Despite its paradigmatic role for the formation of non-standard metal behavior, the stringent conditions required for its emergence have made the observation of the nonmagnetic, orbital 2CK effect in real quantum materials difficult, if not impossible. We report the observation of orbital one- and two-channel Kondo physics in the symmetry-enforced Dirac nodal line (DNL) metals IrO_2 and RuO_2 nanowires and show that the symmetries that enforce the existence of DNLs also promote the formation of nonmagnetic Kondo correlations. Rutile oxide nanostructures thus form a versatile quantum matter platform to engineer and explore intrinsic, interacting topological states of matter.

¹NCTU-RIKEN Joint Research Laboratory, Institute of Physics, National Chiao Tung University, Hsinchu 30010, Taiwan. ²Center for Emergent Functional Matter Science, National Chiao Tung University, Hsinchu 30010, Taiwan. ³International College of Semiconductor Technology, National Chiao Tung University, Hsinchu 30010, Taiwan. ⁴Physikalisches Institut and Bethe Center for Theoretical Physics, Universität Bonn, Nussallee 12, D-53115 Bonn, Germany. ⁵Zhejiang Institute of Modern Physics and Department of Physics, Zhejiang University, Hangzhou 310027, China. ⁶Zhejiang Province Key Laboratory of Quantum Technology and Device, Zhejiang University, Hangzhou 310027, China. ⁷Department of Electrophysics, National Chiao Tung University, Hsinchu 30010, Taiwan. ✉email: stefan.kirchner@correlated-matter.com; jjlin@mail.nctu.edu.tw

Unconventional metallic states and the breakdown of the Landau Fermi liquid paradigm is a central topic in contemporary condensed matter science. A connection with high-temperature superconductivity is experimentally well established but the conditions under which these enigmatic metals form has remained perplexing¹. One of the simplest routes to singular Fermi liquid behavior, at least conceptually, is through two-channel Kondo (2CK) physics^{2–4}. Despite this long-standing interest, 2CK physics has thus far only been demonstrated to arise in carefully designed semiconductor nanodevices in narrow energy and temperature (T) ranges^{5–8}, while claims of its observation in real quantum materials are contentious (see “Discussion” section for details). More recently, the interest in Dirac and Weyl fermions within a condensed matter framework has led to the exploration of the effects of strong spin-orbit coupling (SOC) and of topological states which are rooted in a combination of time-reversal, particle-hole, and space-group symmetries^{9,10}. While there has been considerable progress in understanding weakly correlated topological metals, only a few materials have been identified as realizing topological phases driven by strong electron correlations, which includes the Weyl–Kondo semimetals¹¹. This raises the question if the 2CK counterpart of such a Weyl–Kondo semimetal, featuring an entangled ground state of the low-energy excitations of the 2CK effect with band-structure enforced Dirac or Weyl excitations, could at least in principle be stabilized. Exploring such a possibility, however, hinges on whether the 2CK effect can be stabilized at all in native quantum matter.

In this work we establish that oxygen vacancies (V_{O} 's) in the Dirac nodal line (DNL) materials IrO_2 and RuO_2 drive an orbital Kondo effect. V_{O} 's are prevalent in transition-metal oxides, including, e.g., TiO_2 and SrTiO_3 , and their properties and ramifications have become central research topics as they can lead to an intricate entanglement of spin, orbital, and charge degrees of freedom^{12–15}. The active degree of freedom in the orbital Kondo effect is not a local spin moment but a ‘pseudospin’ formed by orbital degrees of freedom⁴. In IrO_2 and RuO_2 , the orbital Kondo effect is symmetry stabilized by the space-group symmetries of the rutile structure (Fig. 1). Both materials have been characterized as topological metals which feature symmetry-protected DNLs in their Brillouin zones^{16,17}. This provides a link between the formation of the orbital Kondo effect and the presence of DNLs. In IrO_2 a nonmagnetic 2CK ground state ensues, while in RuO_2 the absence of time-reversal symmetry results in an orbital one-channel Kondo (1CK) effect.

The rutile structure type possesses mirror reflection, inversion, and a fourfold rotation (C_4) symmetry which enforce the presence of DNLs in the band structure of rutile oxides¹⁰. Some of these DNLs are protected from gapping out due to large SOC by the non-symmorphic symmetry of the rutile structure^{18,19}. For IrO_2 and RuO_2 this has been recently confirmed by angle-resolved photoemission spectroscopy and band structure studies^{16,17,19}. In the vicinity of V_{O} 's, this set of symmetries promotes the formation of the orbital 1CK and 2CK effect. The emergent Majorana zero mode that accompanies the formation of the 2CK effect is reflected in a singular excitation spectrum above the ground state which generates a \sqrt{T} -dependence of the resistivity $\rho(T)$ below a low- T energy scale²⁰, the Kondo temperature T_{K} . This requires a well-balanced competition of two otherwise independent and degenerate screening channels and makes the 2CK effect extremely difficult to realize, especially in a natural quantum material^{4,21,22}. If one channel dominates over the other, the low- T behavior will be that of conventional fermions. If the 2CK state arises out of orbital Kondo scattering, magnetic-field (B) independence is expected

for field strengths well above T_{K} as long as $g\mu_{\text{B}}B \ll W$, where g is the Landé factor, μ_{B} is the Bohr magneton, and W is the conduction electron half-bandwidth. Our study is based on rutile (MO_2 , $M = \text{Ir, Ru}$) nanowires (NWs) which allow us to combine a high degree of sample characterization with an exceptional measurement sensitivity while probing material properties in the regime where the characteristic sample dimension is much larger than the elastic electron mean free path (cf. Supplementary Note 3). That is, we are concerned with weakly disordered, diffusive metals which are three-dimensional (3D) with respect to the Boltzmann transport, whereas strong correlation effect causes a resistivity anomaly at low T . Table 1 lists the relevant parameters for the NWs studied in this work.

Results

Oxygen vacancies in transition-metal rutiles MO_2 . In Fig. 1a, the vicinity of an V_{O} , denoted $V_{\text{O}1}$, is shown. The metal ions surrounding $V_{\text{O}1}$, labeled $M1$, $M2$, and $M3$, form an isosceles triangle (Fig. 1b). For the sites $M1$ and $M2$, an almost perfect C_{4v} symmetry exists which implies a corresponding degeneracy associated with the two-dimensional irreducible representation of C_{4v} , see Fig. 1c and Supplementary Note 4. In the pristine system, the metal ions are surrounded by oxygen octahedra anchored around the center and the corners of the tetragonal unit cell. The $\pi/2$ angle between adjacent octahedra leads to a fourfold screw axis symmetry. This non-symmorphic symmetry not only protects DNLs in IrO_2 against SOC-induced splitting^{17,19}. It has also been linked to the high electrical conductivity of IrO_2 (ref. 10) and, as we find, is in line with the strong tendency to localize electrons near V_{O} 's required for the formation of orbital Kondo correlations. Moreover, the fourfold screw axis symmetry ensures that the C_4 rotation axes centered at the sites $M1$ and $M2$ near $V_{\text{O}1}$ are not parallel ($\hat{z} \neq \hat{z}$, see Fig. 1d). This enhances the phase space for the orbital Kondo effect over orbital order linking sites $M1$ and $M2$ (see also Supplementary Note 5).

Experimental signatures of orbital 2CK effect in IrO_2 NWs.

Now we turn to our experimental results which, to the best of our knowledge, demonstrate the most convincing realization of the long searched orbital 2CK effect in a solid. Fig. 2 demonstrates the formation of an orbital 2CK effect in IrO_2 NWs. We find that as T decreases from room temperature to approximately a few Kelvin, $\rho(T)$ decreases in all IrO_2 NWs, as expected for typical metallic behavior (cf. Supplementary Note 2). However, below $T \sim 20$ K, $\rho(T)$ displays a \sqrt{T} increase of the $\rho(T)$ upon lowering T over almost two decades in T (!), until a deviation sets in at ~ 0.5 K. We performed systematic thermal annealing studies to adjust the oxygen contents in the NWs, which indicate that the anomalous low- T transport properties are driven by the presence of V_{O} 's (ref. 23 and Supplementary Note 1). This is exemplified in Fig. 2. The top left inset shows a scanning electron microscopy image of NW A. In the oxygenated NW 3 which should contain a negligible amount of V_{O} 's, $\rho(T)$ decreases monotonically with decreasing T , revealing a residual resistivity, $\rho_{\text{B}0}$, below ~ 4 K (top right inset). In contrast, in NWs A, B1 and B2 which contain large amounts of V_{O} 's, $\rho(T)$ increases with decreasing T , manifesting a robust $\rho \propto \sqrt{T}$ law between ~ 0.5 and ~ 20 K. The slope of NW B2 is smaller than that of NW B1, which indicates a decrease in the number density of oxygen vacancies ($n_{V_{\text{O}}}$) due to prolonged aging (for about 5 months) in the atmosphere. The data explicitly demonstrate that the $\rho \propto \sqrt{T}$ behavior is independent of B up to at least 9 T. The observed behavior is consistent with the 2CK effect as indicated by the straight solid lines

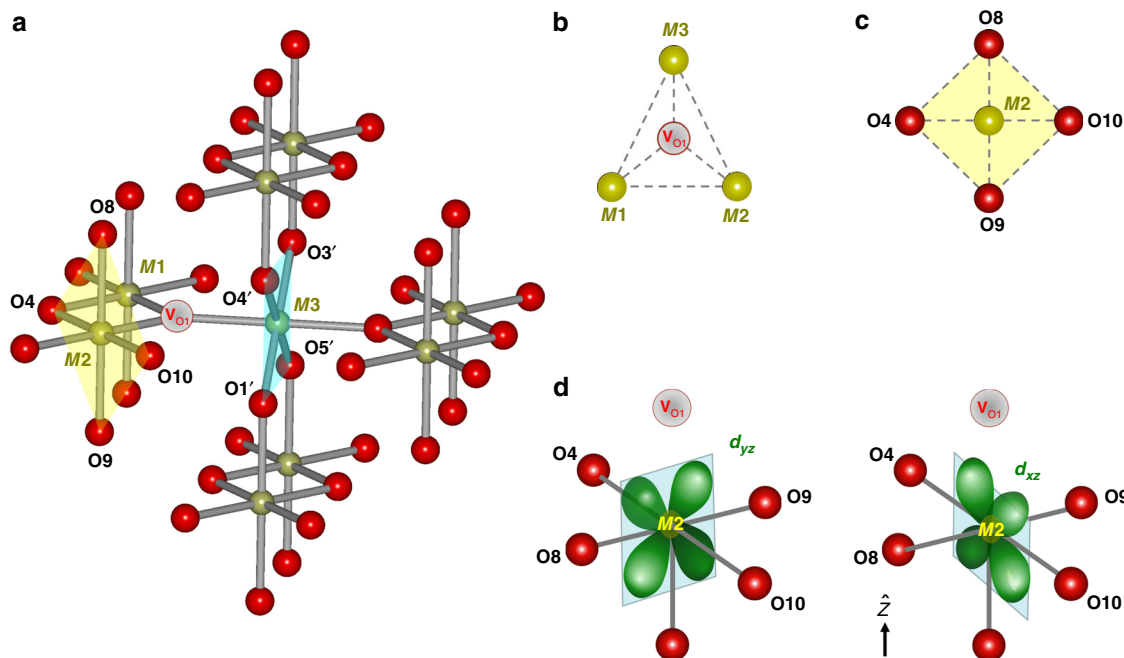


Fig. 1 Atomic arrangement around an oxygen vacancy in MO₂ rutile structure. **a** Schematics for MO₂ in the rutile structure. The olive and red spheres represent transition-metal ions M⁴⁺ and oxygen ions O²⁻, respectively. V_{O1} represents an oxygen vacancy. **b** The metal ions M1, M2, and M3 surrounding V_{O1} form an isosceles triangle. **c** The four oxygen ions surrounding M2, labeled O4, O9, O10, and O8, form an almost perfect planar square (while O1', O5', O3', and O4' only form a rectangle, cf. Supplementary Note 4 for details). **d** The d_{xz} and d_{yz} orbitals at M2 next to V_{O1}, with \hat{z} perpendicular to the O4, O8, O10, and O9 plane, remain essentially degenerate as a result of mirror and C₄ rotation symmetry around M2. (Due to the non-symmorphic rutile structure, $\hat{z} \neq \hat{z}'$, where \hat{z}' is parallel to the C₄ axis at M1.)

Table 1 Relevant parameters for MO₂ NWs.

NW	<i>d</i>	$\rho(300\text{ K})$	ρ_{B0}	$\ell(10\text{ K})$	<i>D</i> (10 K)	ρ_{K0}	<i>T_K</i>	n_{V_O}	$n_{V_O}/n_O(\%)$
IrO ₂ A	130	147	109	2.5	4.2	(0.65)	(20)	-1.9×10^{25}	-0.031
IrO ₂ B1	190	104	73.9	3.7	6.2	(0.72)	(20)	-2.2×10^{25}	-0.036
IrO ₂ B2	190	106	75.0	3.6	6.0	(0.45)	(20)	-1.4×10^{25}	-0.023
RuO ₂ A	53	193	122	2.2	4.0	0.94	3.0	-1.5×10^{25}	-0.025
RuO ₂ B	67	163	120	2.3	4.2	14	12	-2.3×10^{26}	-0.38
RuO ₂ C	54	589	434	0.63	1.2	17	69	-2.7×10^{26}	-0.44
RuO ₂ D	120	245	160	1.7	3.1	7.0	80	-1.1×10^{26}	-0.18
RuO ₂ E	47	761	587	0.47	0.9	30	7.0	-4.8×10^{26}	-0.79

Diameter *d* is in nm, room-temperature resistivity $\rho(300\text{ K})$, residual resistivity ρ_{B0} , and Kondo resistivity in the unitary limit ρ_{K0} are in $\mu\Omega\text{ cm}$, the electron mean free path $\ell(10\text{ K})$ is in nm, the electron diffusion constant *D*(10 K) is in $\text{cm}^2\text{ s}^{-1}$, the Kondo temperature *T_K* is in K, and the number density of oxygen vacancies n_{V_O} is in m^{-3} . n_O denotes the oxygen atom number density in the rutile structure. In all 4-probe configuration for transport measurements, the length between the two voltage probes is $\sim 1\ \mu\text{m}$. The $\ell(10\text{ K})$ and *D* = $1/[\rho e^2 N(E_F)] = \frac{1}{2} v_F \ell$ values are calculated through the free-electron model, where $N(E_F)$ is the density of states at the Fermi energy, and the Fermi velocity $v_F \approx 5.0 \times 10^5$ and $5.5 \times 10^5\ \text{m s}^{-1}$ in IrO₂ and RuO₂, respectively. For each IrO₂ NW, we have empirically taken the ρ_{K0} value to be the maximum value of the measured Kondo resistivity at -0.5 K and $T_K \approx 20\text{ K}$. These values are listed in parentheses. IrO₂ NW B has been measured twice before and after oxygenation in air and labeled B1 (first measurement) and B2 (second measurement).

which are linear fits to the 2CK effect calculated within the dynamical large-*N* method (cf. Supplementary Note 5), with n_{V_O} as an adjustable parameter (see Table 1 for the extracted values and Supplementary Notes 5 and 6 for the extraction method).

Ruling out the 3D electron–electron interaction (EEI) effect.

To complicate matters, the EEI effect in 3D weakly disordered metals generically leads to a \sqrt{T} term in $\rho(T)$ at low *T* (refs. 24,25). Unambiguously establishing that $\rho(T) \sim \sqrt{T}$ indeed originates from 2CK physics thus requires a proper analysis of the EEI effect of the charge carriers. For example, for the NW B1 with $\rho_{B0} = 74\ \mu\Omega\text{ cm}$ and the electron diffusion constant $D \approx 6.2\ \text{cm}^2\text{ s}^{-1}$, the 3D EEI effect would predict a largest possible resistance increase of $\Delta\rho/\rho \approx 2.8 \times 10^{-4}$ as *T* is cooled from 20 to 1 K. Experimentally, we have observed a much larger resistance increase of 5.1×10^{-3} . Furthermore, the 3D EEI effect would predict similar values for the

magnitude of the low-*T* resistivity increase in NWs B1 and B2 to within $\approx 3\%$, due to their ρ_{B0} values differing by $\approx 1\%$ (Table 1). This is definitely incompatible with our observation of a $\approx 50\%$ difference. In addition, we find a deviation from the \sqrt{T} behavior at $\sim 0.5\text{ K}$. If the \sqrt{T} anomaly were caused by the EEI effect, no such deviation should occur (see Supplementary Note 3 for an in-depth analysis of the EEI effect and its 3D dimensionality in our MO₂ NWs).

V_O-driven orbital Kondo scattering in MO₂.

For IrO₂ the valency of the transition-metal ion *M* is close to the nominal valence of +IV in MO₂ (ref. 26). Each V_O generates two defect electrons due to charge neutrality. To minimize Coulomb interaction, the defect electrons will tend to localize at different *M* ions in the vicinity of the V_O. In IrO₂ this results in a nonmagnetic $5d^6$ ground state configuration of the Ir ions. For the electron

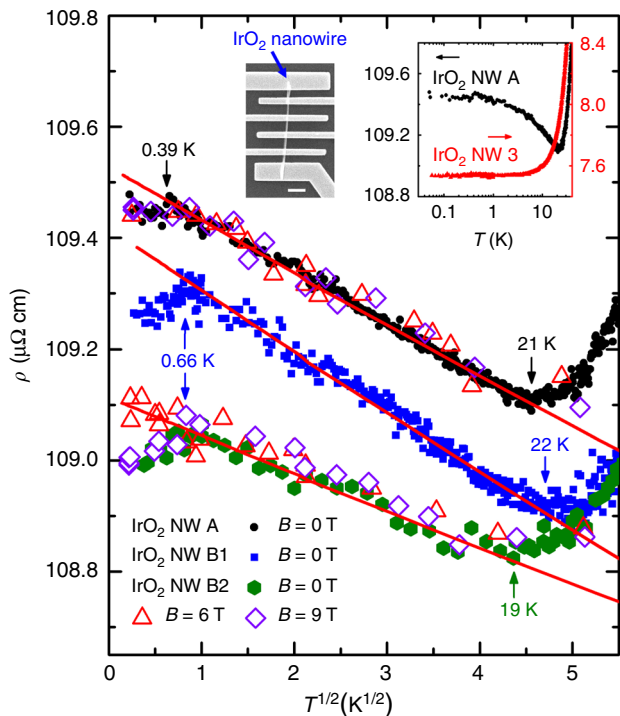


Fig. 2 Orbital 2CK resistivity of IrO₂ NWs. ρ versus \sqrt{T} for IrO₂ NWs A, B1 and B2 in magnetic fields $B = 0, 6,$ and 9 T, as indicated. For clarity, the data of NWs B1 and B2 are shifted by 34.7 and $33.6 \mu\Omega \text{ cm}$, respectively. A $\rho \propto \sqrt{T}$ law, which is B independent, is observed between ~ 0.5 and ~ 20 K in all three NWs. The straight solid lines are linear fits to the 2CK resistivities calculated by the dynamical large- N method (see text). Top left inset: a scanning electron microscopy image of NW A. The scale bar is $1 \mu\text{m}$. Top right inset: Low- T $\rho(T)$ curves of NW A and a reference, oxygenated NW 3 (diameter $d = 330$ nm, $\rho(300 \text{ K}) = 124 \mu\Omega \text{ cm}$).

localizing on ion $M2$ or $M1$ (Fig. 1a), the symmetry of the effective potential implies the almost perfect degeneracy of the orbitals d_{xz} and d_{yz} as defined in Fig. 1d. It is this orbital degeneracy that drives the orbital 2CK effect in IrO₂ where the d_{xz} and d_{yz} form a local pseudospin basis, while the spin-degenerate conduction electrons act as two independent screening channels. Group theoretical arguments ensure that the exchange scattering processes between conduction electrons and pseudospin degree of freedom have a form compatible with the Kondo interaction²⁷ (cf. Supplementary Note 5). Deviations from perfect symmetry which act as a pseudo-magnetic field are expected to become visible at lowest T . This explains the deviations from the \sqrt{T} behavior observed below ~ 0.5 K in Fig. 2. If the two defect electrons localize at sites $M1$ and $M2$, a two-impurity problem might be expected which could lead to inter-site orbital order between the two defect electrons²⁸. The non-symmorphic rutile structure, however, ensures that the C_4 rotation axes centered at the sites $M1$ and $M2$ are not parallel. This together with the local nature of the decomposition provided in Supplementary Eq. (3) (see Supplementary Note 5) favor local orbital Kondo screening in line with our observation. These conclusions are further corroborated by demonstrating tunability of the orbital 2CK effect to its 1CK counterpart.

Experimental signatures of orbital 1CK effect in RuO₂ NWs.

RuO₂ is also a DNL metal with the same non-symmorphic symmetry group as IrO₂ but weaker SOC. In contrast to IrO₂, it lacks time-reversal symmetry^{19,29}. Based on the analysis for IrO₂, we expect that V_{O} 's in RuO₂ will drive an orbital 1CK effect. This

is indeed borne out by our transport data on RuO₂ NWs. Fig. 3a shows the T dependence of the time-averaged Kondo resistivity $\langle \rho_{\text{K}} \rangle$ for NW C, where $\rho_{\text{K}}(T) = \rho(T) - \rho_{\text{B0}}$, and $\langle \dots \rangle$ denotes averaging. (RuO₂ NWs often demonstrate temporal ρ fluctuations. Details can be found in Supplementary Note 2.) At low T , $\langle \rho_{\text{K}} \rangle$ follows the 1CK form³⁰. The inset demonstrates the recovery of a Fermi-liquid ground state with its characteristic $\langle \rho_{\text{K}} \rangle \propto T^2$ behavior below ~ 12 K and unambiguously rules out the 3D EEI effect. Fig. 3b shows $\rho(T)$ of NW E in $B = 0$ and 4 T. For clarity, the $B = 0$ data (black symbols) are averaged over time, while the $B = 4$ T data (red symbols) are non-averaged to demonstrate the temporal fluctuations of the low- T $\rho(T)$ (ref. 31). Note that, apart from the aforementioned much smaller resistance increase as would be predicted by the 3D EEI effect compared with the experimental results in Fig. 3a, b, no \sqrt{T} dependence is detected here. In fact, the low- T resistivity anomalies conform very well to the 1CK scaling form for three decades in T/T_{K} (Fig. 4a). Thus, the 3D EEI effect can be safely ruled out as the root of the observed low- T resistivity anomalies in RuO₂ NWs.

As a further demonstration of the B -field independence, we present in Fig. 3c $\rho(T)$ data for NW A in magnetic fields of strength $B = 0, 3,$ and 5 T. With $T_{\text{K}}^{\text{A}} = 3$ K, NW A has the lowest T_{K} among NWs A–E (Table 1). The data between 50 mK and 10 K, corresponding to $T/T_{\text{K}} = 0.017$ – 3.3 , can be well described by the 1CK function (solid curve). The dash-dotted curves depict the magnetoresistance predicted by the spin- $\frac{1}{2}$ Kondo impurity model³⁰ with $g\mu_{\text{B}}B/k_{\text{B}}T_{\text{K}} = 1.0, 2.0,$ and 4.1 , as indicated, where k_{B} is the Boltzmann constant. Our experimental data clearly demonstrate B independence, ruling out a magnetic origin of this phenomenon.

We remark on the relation between the residual resistivity ρ_{B0} and the concentration of orbital Kondo scatterers $n_{V_{\text{O}}}$ extracted from ρ_{K0} , the Kondo contribution to the $\rho(T \rightarrow 0)$ (see Supplementary Note 6), for RuO₂ NWs. With the exception of NW B, our data indicate an approximately linear relation between $n_{V_{\text{O}}}$ and ρ_{B0} (Table 1 and Supplementary Fig. 3). It is not unexpected that the approximately linear relation between ρ_{B0} and $n_{V_{\text{O}}}$ holds for larger impurity concentrations, corresponding to larger values of ρ_{B0} as all defects, screened dynamic and static defects, contribute to ρ_{B0} . This relation strongly demonstrates that the low- T resistivity anomalies are indeed due to V_{O} -driven orbital Kondo effect. (We focus on RuO₂ NWs because of the larger number of samples with a larger variation of ρ_{B0} values compared with IrO₂ NWs).

Comparison of 2CK and 1CK $\rho(T)$ curves. Figure 4a demonstrates that $\langle \rho_{\text{K}} \rangle / \rho_{\text{K0}}$ for RuO₂ NWs follow the universal 1CK scaling over three decades in T/T_{K} while T_{K} ranges from 3 to 80 K! To further substantiate the subtle but distinct differences between the \sqrt{T} dependence of the 2CK behavior in IrO₂ NWs from the 1CK scaling form, we plot $\langle \rho_{\text{K}} \rangle / \rho_{\text{K0}}$ as a function of \sqrt{T}/T_{K} for IrO₂ NWs A and B1, together with RuO₂ NWs B–E and the 1CK function, in Fig. 4b, c, respectively. (The value for ρ_{K0} was identified with the maximum values of the measured $\rho_{\text{K}}(T)$ anomalies.) Fig. 4d illustrates that a dilute system of 2CK scattering centers immersed in a metallic host indeed displays a \sqrt{T} term in its low- T $\rho(T)$. This \sqrt{T} power-law behavior is determined by the leading irrelevant operator near the 2CK fixed point³² and captured by the dynamical large- N method^{33–35}.

Discussion

Despite the ubiquitous appearance of magnetic Kondo scattering in real quantum materials³⁶, no convincing demonstration of the orbital Kondo effect³⁷ or the 2CK effect^{22,38} exists. Many claims rest on a model of two-level systems immersed in a metallic host as a

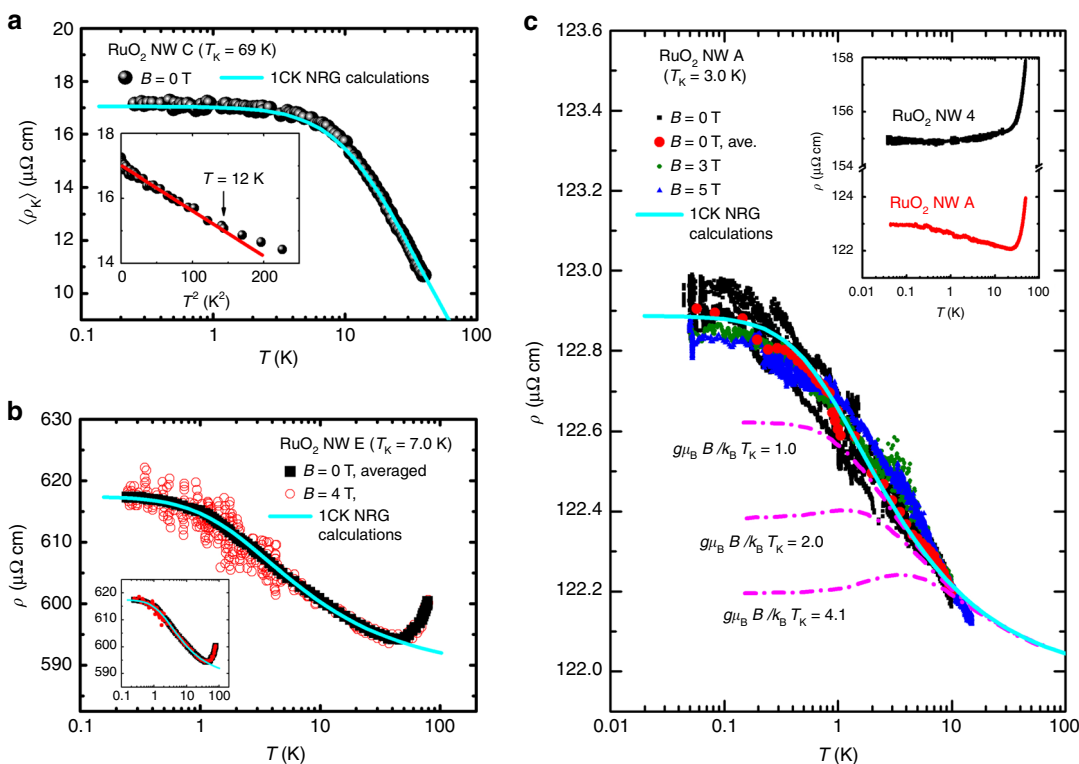


Fig. 3 Orbital 1CK resistivity of RuO₂ NWs. **a** Time-averaged Kondo resistivity $\langle \rho_K \rangle$ versus $\log T$ for NW C. The straight line in the inset, which shows a low- T zoom-in, is a guide to the eye. **b** ρ versus $\log T$ in $B = 0$ and 4 T for NW E. For clarity, the $B = 0$ data are time-averaged, while the 4-T data are non-averaged to demonstrate the temporal resistivity fluctuations at low T . The inset shows the time-averaged $B = 4$ T data (red symbols), which closely overlap the $B = 0$ data. **c** ρ versus $\log T$ for NW A in $B = 0, 3,$ and 5 T. Occasional resistivity jumps, or random telegraph noise, are observed. The dash-dotted curves depict the magnetoresistance predicted by the spin- $\frac{1}{2}$ Kondo impurity model (see text). Note that the experimental data are independent of B . Inset: Low- T $\rho(T)$ curves of NW A and a reference, oxygenated NW 4 ($d = 150$ nm, $\rho(300$ K) = 336 $\mu\Omega$ cm). In **a–c**, the solid curve shows the $B = 0$ numerical renormalization group result for 1CK effect⁵⁹.

possible route to 2CK physics^{3,4}. Theoretical arguments have, however, made it clear that this is not a viable route to nonmagnetic Kondo scattering^{22,38}. Moreover, the creation of scattering centers in a real quantum material necessarily places the system in the weakly disordered regime where a conductance anomaly, the Altshuler–Aronov correction, occurs whose T dependence can be mistaken for a 2CK signature, see, e.g., refs. ^{39–42}. Dilution studies on common Kondo lattice systems^{43,44}, on the other hand, typically create disorder distributions of Kondo temperatures that may result in a behavior of observables, which can easily be mistaken for that of a generic non-Fermi liquid⁴⁵.

We have shown that the low- T resistivity anomaly in the transition-metal rutile IrO₂ is caused by V_O 's, demonstrating key signatures of an orbital 2CK effect and ruling out alternative explanations due to, e.g., the EEI effect. The most convincing argument in favor of 2CK physics would be the demonstration of direct tunability of 2CK physics to 1CK physics upon breaking the channel degeneracy. This is difficult, as the channel degeneracy is protected by time-reversal symmetry. A perhaps less direct, yet complementary, demonstration of this tunability is provided by our results for RuO₂ NWs which develop an orbital 1CK effect. In RuO₂, the antiferromagnetic order breaks the channel degeneracy. Our analysis also indicates that the underlying symmetries which support the existence of DNLs in the Brillouin zones of both transition-metal rutiles also aid the formation of orbital 2CK and 1CK physics.

Materials condensing in the rutile structure type and its derivatives form an abundant and important class that has helped shaping our understanding of correlated matter. The metal-insulator transition in VO₂, e.g., has been known for 60 years⁴⁶,

yet its dynamics is still not fully understood⁴⁷. The demonstration that the non-symmorphic rutile space group supports a V_O -driven orbital Kondo effect in MO₂ holds promise for the realization of novel states of matter. The potential richness of orbital Kondo physics, e.g., on superconducting pairing, was recently pointed out in ref. ³⁷ but may be even richer when considering the possibility of its interplay with topological band structures. Specifically, we envision the creation of a 2CK non-symmorphic superlattice of V_O 's in IrO₂ where the 2CK Majorana modes entangle with the band structure-enforced Dirac excitations forming a strongly correlated topological non-Fermi liquid state. Understanding its properties will foster deeper insights into the interplay of topology with strong correlations beyond the usual mean field treatment. The theoretical approach to this non-symmorphic superlattice is reminiscent of the topologically garnished strong-coupling fixed-point pioneered in the context of Weyl–Kondo semimetals^{11,48}, suitably generalized to capture the intermediate coupling physics of the 2CK effect and its low- T excitations. The fabrication of superlattices of Kondo scattering centers has already been demonstrated⁴⁹ while defect engineering of vacancy networks, including V_O networks is currently explored in a range of materials^{50,51}. The specifics of this unique state and its manufacturing are currently being explored.

Methods

NW growth. IrO₂ NWs were grown by the metal-organic chemical vapor deposition method, using (MeCp)Ir(COD) supplied by Strem Chemicals as the source reagent. Both the precursor reservoir and the transport line were controlled in the temperature range of 100–130 °C to avoid precursor condensation during the vapor-phase transport. High purity O₂, with a flow rate of 100 sccm, was used as the carrier gas and reactive gas. During the deposition, the substrate temperature

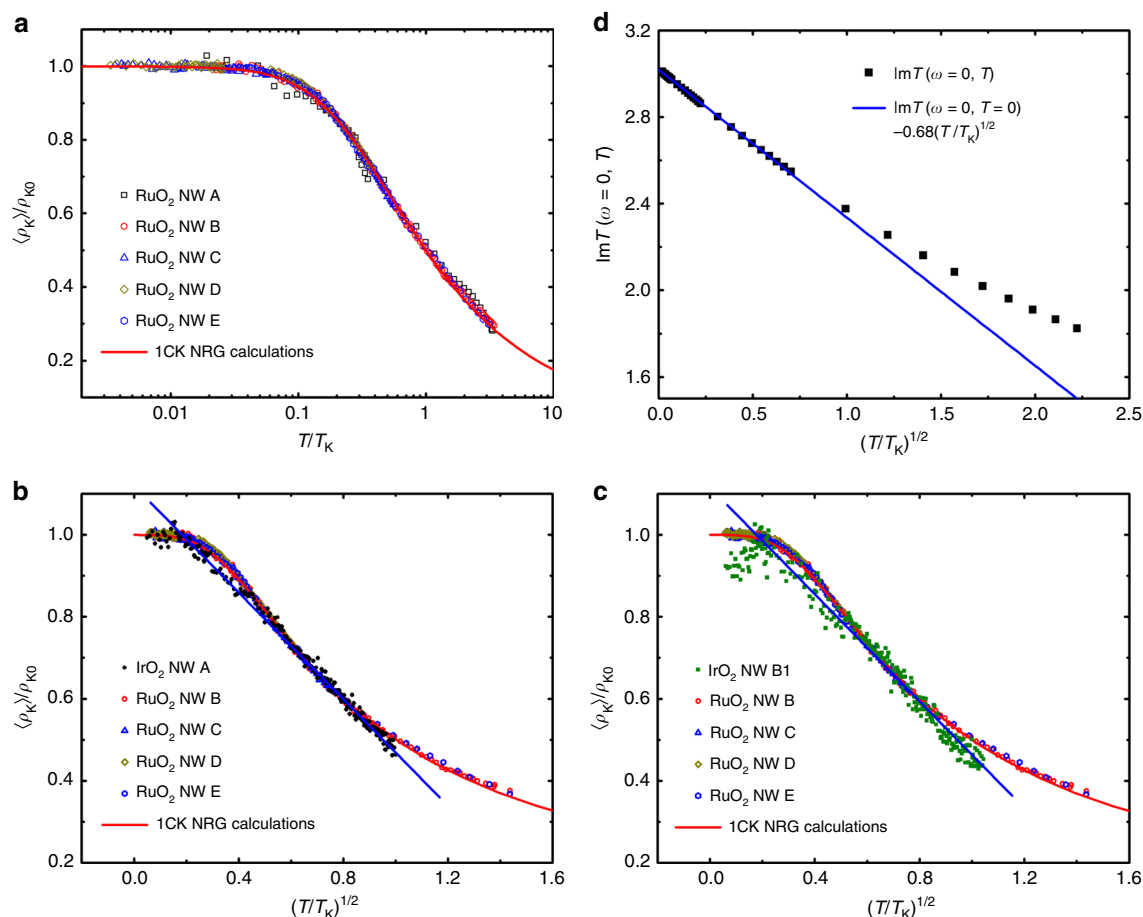


Fig. 4 Comparison of 2CK and 1CK resistivities. **a** Normalized Kondo resistivity $\langle \rho_K \rangle / \rho_{K0}$ versus T/T_K for RuO₂ NWs A-E manifests the 1CK scaling form (solid curve) for over three decades of reduced temperature. **b** $\langle \rho_K \rangle / \rho_{K0}$ versus $\sqrt{T/T_K}$ for IrO₂ NW A and RuO₂ NWs B-E. The data of IrO₂ NW A obeys a \sqrt{T} law between 0.39 and 21 K. For clarity, the experimental data points for RuO₂ NWs are plotted with small open symbols. **c** $\langle \rho_K \rangle / \rho_{K0}$ of IrO₂ NW B1 obeys a $\sqrt{T/T_K}$ law between 0.66 and 22 K, distinctively deviating from the 1CK function. **d** Results for the resistivity of a diluted system of 2CK impurities in a metallic host evaluated using a dynamical large- N limit (black symbols), which follows a $\sqrt{T/T_K}$ law at low T (see text and Supplementary Note 5). The ordinate is plotted in unit of half-bandwidth $W = 4$ eV (ref. 60).

was kept at ≈ 350 °C and the chamber pressure was held at ≈ 17 torr to grow NWs^{52,53}. Selected-area electron diffraction patterns⁵² and X-ray diffraction (XRD) patterns⁵⁴ revealed a single-crystalline rutile structure.

RuO₂ NWs were grown by the thermal evaporation method based on the vapor-liquid-solid mechanism, with Au nanoparticles as catalyst. A quartz tube was inserted in a furnace. A source material of stoichiometric RuO₂ powder (Aldrich, 99.9%) was placed in the center of the quartz tube and heated to 920–960 °C. During the NW growth, an O₂ gas was introduced into the quartz tube and the chamber was maintained at a constant pressure of ≈ 2 torr. Silicon wafer substrates were loaded at the downstream end of the quartz tube, where the temperature was kept at 450–670 °C (ref. 55). The morphology and lattice structure of the NWs were studied using XRD and high-resolution transmission electron microscopy (HR-TEM). The XRD patterns demonstrated a rutile structure⁵⁵, and the HR-TEM images revealed a polycrystalline lattice structure⁵⁶.

Electrical measurements. Submicron Cr/Au (10/100 nm) electrodes for 4-probe $\rho(T)$ measurements were fabricated by the standard electron-beam lithography technique. The electrode fabrication was done after the thermal treatment (annealing and/or oxygenation) of each NW was completed. To avoid electron overheating, the condition for equilibrium, $eV_s \ll k_B T$, was assured in all resistance measurements⁵⁷, where e is the electronic charge, and V_s is the applied voltage across the energy relaxation length. The electrical-transport measurements were performed on a BlueFors LD-400 dilution refrigerator equipped with room-temperature and low-temperature low-pass filters. The electron temperature was calibrated down to $\lesssim 50$ mK. In several cases (RuO₂ NWs B-E), the measurements were performed on an Oxford Heliox ³He cryostat with a base temperature of ≈ 250 mK. The magnetic fields were supplied by superconducting magnets and applied perpendicular to the NW axis in all cases.

Data availability

All data collected or analyzed during this study is available in the main text or the Supplementary Information material.

Code availability

Details on the numerics is available upon request from the authors.

Received: 7 April 2020; Accepted: 18 August 2020;

Published online: 21 September 2020

References

- Keimer, B., Kivelson, S. A., Norman, M. R., Uchida, S. & Zaanen, J. From quantum matter to high-temperature superconductivity in copper oxides. *Nature* **518**, 179–186 (2015).
- Nozières, P. & Blandin, A. Kondo effect in real metals. *J. Phys.* **41**, 193–211 (1980).
- Vladar, K. & Zawadowski, A. Theory of the interaction between electrons and the two-level system in amorphous metals. I. Noncommutative model Hamiltonian and scaling of first order. *Phys. Rev. B* **28**, 1564–1581 (1983).
- Cox, D. L. & Zawadowski, A. Exotic Kondo effects in metals: magnetic ions in a crystalline electric field and tunnelling centres. *Adv. Phys.* **47**, 599–942 (1998).
- Potok, R. M., Rau, I. G., Shtrikman, H., Oreg, Y. & Goldhaber-Gordon, D. Observation of the two-channel Kondo effect. *Nature* **446**, 167–171 (2007).

6. Keller, A. J. et al. Universal Fermi liquid crossover and quantum criticality in a mesoscopic system. *Nature* **526**, 237 (2015).
7. Iftikhar, Z. et al. Two-channel Kondo effect and renormalization flow with macroscopic quantum charge states. *Nature* **526**, 233 (2015).
8. Iftikhar, Z. et al. Quantum criticality and super-ballistic transport in a charge Kondo circuit. *Science* **360**, 1315 (2018).
9. Burkov, A. A. Topological semimetals. *Nat. Mater.* **15**, 1145–1148 (2016).
10. Yang, S.-Y. et al. Symmetry demanded topological nodal-line materials. *Adv. Phys.: X* **3**, 1414631 (2018).
11. Dzsaber, S. et al. Kondo insulator to semimetal transformation tuned by spin-orbit coupling. *Phys. Rev. Lett.* **118**, 246601 (2017).
12. Ourmazd, A. & Spence, J. C. H. Detection of oxygen ordering in superconducting cuprates. *Nature* **329**, 425–427 (1987).
13. Lin, C. & Demkov, A. A. Electron correlation in oxygen vacancy in SrTiO₃. *Phys. Rev. Lett.* **111**, 217601 (2013).
14. Lin, C., Shin, D. & Demkova, A. A. Localized states induced by an oxygen vacancy in rutile TiO₂. *J. Appl. Phys.* **117**, 225703 (2015).
15. Lechermann, F., Heckel, W., Kristanovski, O. & Müller, S. Oxygen-vacancy driven electron localization and itinerancy in rutile-based TiO₂. *Phys. Rev. B* **95**, 195159 (2017).
16. Jovic, V. et al. Dirac nodal lines and flat-band surface state in the functional oxide RuO₂. *Phys. Rev. B* **98**, 241101 (2018).
17. Nelson, J. N. et al. Dirac nodal lines protected against spin-orbit interaction in IrO₂. *Phys. Rev. Mater.* **3**, 064205 (2019).
18. Zhao, Y. X. & Schnyder, A. P. Nonsymmorphic symmetry-required band crossings in topological semimetals. *Phys. Rev. B* **94**, 195109 (2016).
19. Sun, Y., Zhang, Y., Liu, C.-X., Felsner, C. & Yan, B. Dirac nodal lines and induced spin Hall effect in metallic rutile oxides. *Phys. Rev. B* **95**, 235104 (2017).
20. Coleman, P., Ioffe, L. B. & Tselik, A. M. Simple formulation of the two-channel Kondo model. *Phys. Rev. B* **52**, 6611–6627 (1995).
21. Moustakas, A. L. & Fisher, D. S. Two-channel Kondo physics from tunneling impurities with triangular symmetry. *Phys. Rev. B* **55**, 6832–6846 (1997).
22. Aleiner, I. & Controzzi, D. Nonexistence of a strong coupling two-channel Kondo fixed point for microscopic models of tunneling centers. *Phys. Rev. B* **66**, 045107 (2002).
23. Yeh, S.-S., Gao, K. H., Wu, T.-L., Su, T.-K. & Lin, J.-J. Activation energy distribution of dynamical structural defects in RuO₂ films. *Phys. Rev. Appl.* **10**, 034004 (2018).
24. Altshuler, B. L. & Aronov, A. G. *Electron-electron Interaction in Disordered Conductors*, book section 1 (North-Holland Physics Publishing, Amsterdam, The Netherlands, 1985).
25. Lee, P. A. & Ramakrishnan, T. V. Disordered electronic systems. *Rev. Mod. Phys.* **57**, 287–337 (1985).
26. Ping, Y., Galli, G. & Goddard, W. A. Electronic structure of IrO₂: the role of the metal d orbitals. *J. Phys. Chem. C* **119**, 11570–11577 (2015).
27. Cox, D. L. Quadrupolar Kondo effect in uranium heavy-electron materials? *Phys. Rev. Lett.* **59**, 1240–1243 (1987).
28. Mitchell, A. K., Sela, E. & Logan, D. E. Two-channel Kondo physics in two-impurity Kondo models. *Phys. Rev. Lett.* **108**, 086405 (2012).
29. Zhu, Z. H. et al. Anomalous antiferromagnetism in metallic RuO₂ determined by resonant X-ray scattering. *Phys. Rev. Lett.* **122**, 017202 (2019).
30. Costi, T. A. Kondo effect in a magnetic field and the magnetoresistivity of Kondo alloys. *Phys. Rev. Lett.* **85**, 1504–1507 (2000).
31. Lien, A.-S., Wang, L. Y., Chu, C. S. & Lin, J.-J. Temporal universal conductance fluctuations in RuO₂ nanowires due to mobile defects. *Phys. Rev. B* **84**, 155432 (2011).
32. Affleck, I. & Ludwig, A. W. Exact conformal-field-theory results on the multichannel Kondo effect: single-fermion Green's function, self-energy, and resistivity. *Phys. Rev. B* **48**, 7297–7321 (1993).
33. Parcollet, O. & Georges, A. Overscreened multichannel SU(N) Kondo model: large-N solution and conformal field theory. *Phys. Rev. B* **58**, 3794–3813 (1998).
34. Cox, D. & Ruckenstein, A. Spin-flavor separation and non-Fermi-liquid behavior in the multichannel Kondo problem: a large-N approach. *Phys. Rev. Lett.* **71**, 1613–1616 (1993).
35. Zamani, F., Chowdhury, T., Ribeiro, P., Ingersent, K. & Kirchner, S. Quantum criticality in the two-channel pseudogap Anderson model: a test of the non-crossing approximation. *Phys. Status Solidi B* **250**, 547–552 (2013).
36. Hewson, A. C. *The Kondo Problem to Heavy Fermions*. (Cambridge University Press, Cambridge, 1993).
37. Kuramoto, Y. Composite electronic orders induced by orbital Kondo effect. *Sci. Bull.* **61**, 1563 (2016).
38. Moustakas, A. & Fisher, D. Prospects for non-Fermi-liquid behavior of a two-level impurity in a metal. *Phys. Rev. B* **53**, 4300–4315 (1996).
39. Zhu, L. J., Nie, S. H., Xiong, P., Schlottmann, P. & Zhao, J. H. Orbital two-channel Kondo effect in epitaxial ferromagnetic Li₀-MnAl films. *Nat. Commun.* **7**, 10817 (2016).
40. Zhu, L. J. & Zhao, J. H. Anomalous resistivity upturn in epitaxial L₂-Co₂MnAl films. *Sci. Rep.* **7**, 42931 (2017).
41. Cichorek, T. et al. Two-channel Kondo physics due to As vacancies in the layered compound ZrAs_{1.58}Se_{0.39}. *Phys. Rev. Lett.* **117**, 106601 (2016).
42. Gnida, D. Comment on two-channel Kondo physics due to As vacancies in the layered compound ZrAs_{1.58}Se_{0.39}. *Phys. Rev. Lett.* **118**, 259701 (2017).
43. Nicklas, M. et al. Charge-doping-driven evolution of magnetism and non-Fermi-liquid behavior in the filled skutterudite CePt₄Ge_{12-x}Sb_x. *Phys. Rev. Lett.* **109**, 236405 (2012).
44. Yamane, Y. et al. Single-site non-Fermi-liquid behaviors in a diluted 4f² system Y_{1-x}Pr_xIr₂Zn₂₀. *Phys. Rev. Lett.* **121**, 077206 (2018).
45. Miranda, E., Dobrosavljević, V. & Kotliar, G. Disorder-driven non-Fermi-liquid behavior in Kondo alloys. *Phys. Rev. Lett.* **78**, 290–293 (1997).
46. Morin, F. J. Oxides which show a metal-to-insulator transition at the Néel temperature. *Phys. Rev. Lett.* **3**, 34–36 (1959).
47. Wall, S. et al. Ultrafast disordering of vanadium dimers in photoexcited VO₂. *Science* **362**, 572–576 (2018).
48. Lai, H.-H., Grefe, S. E., Paschen, S. & Si, Q. Weyl-Kondo semimetal in heavy-fermion systems. *PNAS* **115**, 93–97 (2018).
49. Goh, S. K. et al. Anomalous upper critical field in CeCoIn₅/YbCoIn₅ superlattices with a Rashba-type heavy fermion interface. *Phys. Rev. Lett.* **109**, 157006 (2012).
50. Simonov, A. et al. Hidden diversity of vacancy networks in Prussian blue analogues. *Nature* **578**, 256–260 (2020).
51. Lai, F. et al. Oxygen vacancy engineering in spinel-structured nanosheet wrapped hollow polyhedra for electrochemical nitrogen fixation under ambient conditions. *J. Mater. Chem. A* **8**, 1652–1659 (2020).
52. Chen, R.-S. & Huang, Y.-S. Field emission from vertically aligned conductive IrO₂ nanorods. *Appl. Phys. Lett.* **84**, 1552 (2004).
53. Lin, Y. H. et al. Electrical transport studies of individual IrO₂ nanorods and their nanorod contacts. *Nanotechnology* **19**, 045711 (2008).
54. Chen, R.-S. et al. Growth and characterization of vertically aligned self-assembled IrO₂ nanotubes on oxide substrates. *J. Cryst. Growth* **271**, 105–112 (2004).
55. Liu, Y.-L. et al. Growth of single-crystalline RuO₂ nanowires with one- and two-nanocontact electrical characterizations. *Appl. Phys. Lett.* **90**, 013105 (2007).
56. Yeh, S.-S., Chang, W.-Y. & Lin, J.-J. Probing nanocrystalline grain dynamics in nanodevices. *Sci. Adv.* **3**, e1700135 (2017).
57. Huang, S. M., Lee, T. C., Akimoto, H., Kono, K. & Lin, J. J. Observation of strong electron dephasing in highly disordered Cu₉₃Ge₄Au₃ thin films. *Phys. Rev. Lett.* **99**, 046601 (2007).
58. Momma, K. & Izumi, F. VESTA3 for three-dimensional visualization of crystal, volumetric and morphology data. *J. Appl. Crystallogr.* **44**, 1272–1276 (2011).
59. Costi, T. A., Hewson, A. C. & Zlatic, V. Transport coefficients of the Anderson model via the numerical renormalization group. *Matter* **6**, 2519–2558 (1994).
60. de Almeida, J. S. & Ahuja, R. Electronic and optical properties of RuO₂ and IrO₂. *Phys. Rev. B* **73**, 165102 (2006).

Acknowledgements

The authors are grateful to F. R. Chen, J. J. Kai, and the late Y. S. Huang for growing RuO₂ and IrO₂ NWs, S. P. Chiu for experimental assistance, T. A. Costi for providing the 1CK scaling curve from NRG calculations, and Q. Si, A. M. Chang, C. H. Chung, and S. Wirth for helpful discussions. Figure 1a was produced with the help of VESTA⁵⁸. This work was supported by Ministry of Science and Technology, Taiwan (grant Nos. MOST 106-2112-M-009-007-MY4, 108-3017-F-009-004, and 108-2811-M-009-500) and the Center for Emergent Functional Matter Science of National Chiao Tung University from The Featured Areas Research Center Program within the framework of the Higher Education Sprout Project by the Ministry of Education (MOE) in Taiwan. F.Z. and J.K. acknowledge financial support by the Deutsche Forschungsgemeinschaft (DFG) through SFB/TR 185 (277625399) and the Cluster of Excellence ML4Q (390534769). Work at Zhejiang University was in part supported by the National Key R&D Program of the MOST of China, grant No. 2016YFA0300202 and the National Science Foundation of China, grant No. 11774307.

Author contributions

S.S.Y., S.K., and J.J.L. conceived the experiment. S.S.Y. and A.S.L. carried out electrical transport measurements. T.K.S., C.C.L., and A.S.L. fabricated 4-probe NW devices with thermal treatments. F.Z. performed dynamical large-N calculations. J.K. provided theoretical support. S.S.Y., S.K., and J.J.L. analyzed and explained the data, and wrote the paper.

Competing Interests

The authors declare no competing interests.

Additional information

Supplementary information is available for this paper at <https://doi.org/10.1038/s41467-020-18407-7>.

Correspondence and requests for materials should be addressed to S.K. or J.-J.L.

Peer review information *Nature Communications* thanks the anonymous reviewer(s) for their contribution to the peer review of this work. Peer reviewer reports are available.

Reprints and permission information is available at <http://www.nature.com/reprints>

Publisher's note Springer Nature remains neutral with regard to jurisdictional claims in published maps and institutional affiliations.



Open Access This article is licensed under a Creative Commons Attribution 4.0 International License, which permits use, sharing, adaptation, distribution and reproduction in any medium or format, as long as you give appropriate credit to the original author(s) and the source, provide a link to the Creative Commons license, and indicate if changes were made. The images or other third party material in this article are included in the article's Creative Commons license, unless indicated otherwise in a credit line to the material. If material is not included in the article's Creative Commons license and your intended use is not permitted by statutory regulation or exceeds the permitted use, you will need to obtain permission directly from the copyright holder. To view a copy of this license, visit <http://creativecommons.org/licenses/by/4.0/>.

© The Author(s) 2020